Nano Research 2016, 9(12): 3735–3746
DOI 10.1007/s12274-016-1244-1
Research Article

ISSN 1998-0124
CN 11-5974/O4

A hybrid carbon aerogel with both aligned and interconnected pores as interlayer for high-performance lithium–sulfur batteries

Mingkai Liu[1,2], Zhibin Yang[2], Hao Sun[2], Chao Lai[1], Xinsheng Zhao[3], Huisheng Peng[2] (✉), and Tianxi Liu[1,4] (✉)

[1] *School of Chemistry and Chemical Engineering, Jiangsu Key Laboratory of Green Synthetic Chemistry for Functional Materials, Jiangsu Normal University, Xuzhou 221116, China*
[2] *State Key Laboratory of Molecular Engineering of Polymers, Department of Macromolecular Science, and Laboratory of Advanced Materials, Fudan University, Shanghai 200438, China*
[3] *School of Physics and Electronic Engineering, Jiangsu Normal University, Xuzhou 221116, China*
[4] *State Key Laboratory for Modification of Chemical Fibers and Polymer Materials, College of Materials Science and Engineering, Donghua University, Shanghai 201620, China*

Received: 23 June 2016
Revised: 29 July 2016
Accepted: 2 August 2016

KEYWORDS

lithium–sulfur battery,
carbon aerogel,
interlayer,
aligned and interconnected pores,
trapped polysulfide

ABSTRACT

The soluble nature of polysulfide species created on the sulfur electrode has severely hampered the electrochemical performance of lithium–sulfur (Li–S) batteries. Trapping and anchoring polysulfides are promising approaches for overcoming this issue. In this work, a mechanically robust, electrically conductive hybrid carbon aerogel (HCA) with aligned and interconnected pores was created and investigated as an interlayer for Li–S batteries. The hierarchical cross-linked networks constructed by graphene sheets and carbon nanotubes can act as an "internet" to capture the polysulfide, while the micro- and nano-pores inside the aerogel can facilitate quick penetration of the electrolyte and rapid transport of lithium ions. As advantages of the unique structure and excellent accommodation of the volume change of the active materials, a high specific capacity of 1,309 mAh·g^{-1} at 0.2 C was achieved for the assembled Li–S battery, coupled with good rate performance and long-term cycling stability (78% capacity retention after 600 cycles at 4 C).

1 Introduction

Next-generation rechargeable energy storage systems with high energy and power densities, long cycle life, low cost, and high safety are in great demand due to the escalating requirements of various applications such as electric vehicles and electronic devices [1–7]. A variety of energy storage devices has thus been extensively explored in recent years. Among them, the lithium–sulfur (Li–S) battery represents a promising

---

Address correspondence to Huisheng Peng, penghs@fudan.edu.cn; Tianxi Liu, txliu@fudan.edu.cn

candidate due to its high theoretical energy density (2,567 Wh·kg^{-1}) and specific capacity (1,675 mAh·g^{-1}), as well as its environmental friendliness [8–12]. Nonetheless, practical application of Li–S batteries is severely restricted by several challenges. Firstly, the intrinsically poor electrical conductivity of sulfur and its discharge products (Li_2S/Li_2S_2) leads to inefficient utilization of the active materials [13–16]. Secondly, long-chain lithium polysulfides (Li_2S_n, $4 \le n \le 8$), which are reaction intermediaries with high solubility, generally migrate between the anode and cathode during cycling due to their notorious "shuttle" mechanism in organic electrolytes. This inevitably causes low utilization of the active materials with severe anode corrosion [17]. Thirdly, volume change (~80%) occurs during the charge/discharge processes due to the density difference between sulfur (2.03 g·cm^{-3}) and Li_2S (1.66 g·cm^{-3}), which results in unstable electrochemical contact between sulfur and the electrode matrix [18–22]. These drawbacks lead to poor rate capability, low Coulombic efficiency, low specific capacity, and limited cycle life.

Introduction of a barrier layer between the sulfur cathode and the separator is proposed as a method to decrease the "shuttle" side-effect and enhance the utilization of active sulfur [5, 23, 24]. Although various materials and structures, such as porous edifices, have been studied for use as the interlayer, the electrochemical performance of Li–S batteries is way below what is expected [5, 13, 17–19, 25–27]. The transport of lithium ions is generally hindered during the charge–discharge process, which results in limited energy storage performance, specifically, poor cyclic stability. It remains an important challenge to create novel porous structures to facilitate the transport of lithium ions.

Nature may provide inspiration for resolving the aforementioned challenges. For instance, the blood circulation systems of the mammal contain arteries, veins, and capillaries that support rapid transport and sufficient delivery of blood to organs and tissues. As another example, a variety of nutrients is rapidly and effectively transported through the trunk and branch in plants. These hierarchical structures may also provide inspiration for the development of Li–S batteries that also require rapid and efficient transport of ions and molecules.

In this study, a mechanically robust, electrically conductive hybrid carbon aerogel (HCA) with hierarchical pores is created from carbon nanotubes (CNTs) and reduced graphene oxide (RGO) sheets for high-performance Li–S batteries (Fig. 1). The aligned and cross-linked CNTs produce both aligned micrometer-sized and interconnected nanometer-sized pores that facilitate the transport of electrons and lithium ions and prevent the migration of polysulfide materials with the assistance of RGO sheets. The aligned large and interconnected small pores also effectively accommodate volume changes of the active materials. Therefore, a high specific capacity of 1,309 mAh·g^{-1} at 0.2 C could be obtained for the Li–S battery, and superior cyclic stability with retention of ~78% of the capacity after 600 charge–discharge cycles was also achieved at a high current density of 4 C. Furthermore, the HCA materials used herein can be produced on a large scale with low cost and high efficiency, which

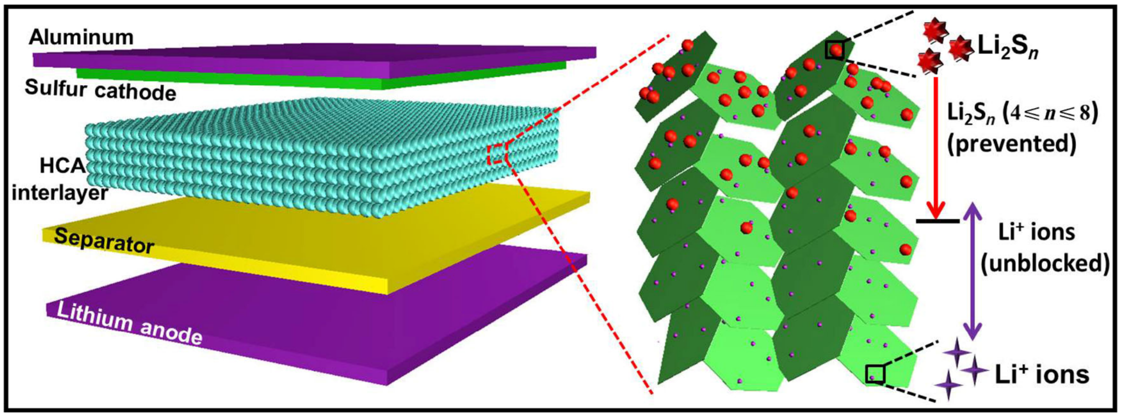

Figure 1 Schematic illustration of the structure of Li–S battery with HCA interlayer and its inhibitory effect on diffusion of polysulfides.

opens up a new avenue for the advancement of energy-based materials and devices.

2 Experimental

2.1 Materials

Graphite powder with a particle size of ~500 μm was obtained from Qingdao Henglide Graphite Co., Ltd. Pristine CNTs with diameters of 30–50 nm and lengths of ~10 μm were acquired from Aladdin Industrial Inc. Hydrazine hydrate (85%), concentrated H_2SO_4 (98%), $KMnO_4$, and hydrogen peroxide (30%) were provided by Sinopharm Chemical Reagent Co., Ltd.

2.2 Preparation of lightweight, electrically conductive hybrid carbon aerogel film

Graphene oxide (GO) sheets were synthesized according to the previously reported method [3]. An appropriate amount of CNTs was dispersed in GO solution under ultrasonication with a weight ratio of 1/2, leading to successful formation of the GO/CNT hybrid with a total weight concentration of 3 wt.%. The hybrid suspension was poured into a planar aluminum foil container (8 cm in diameter), the side of which was packed with polyfoam, and the container was then placed above liquid nitrogen. This led to formation of a uniaxial thermal gradient, and the hybrid dispersion was unidirectionally frozen from the bottom to the top. The resulting GO/CNT hybrid film was freeze-dried for 24 h under vacuum (lower than 20 Pa), followed by a chemical reduction process with hydrazine vapor at 95 °C for 24 h before drying under vacuum at 100 °C. The thickness of the RGO/CNT hybrid film could be easily controlled by changing the volume of the GO/CNT dispersion in the foil container, and carbon aerogel films with a thickness of about 1.5 mm were used in this work.

2.3 Characterization

Scanning electron microscopy (SEM) images were obtained by using a Zeiss Ultra-55 system. Transmission electron microscopy (TEM) images were acquired using a Jeol JEM 2100 instrument operated at 200 kV. The sheet resistance was characterized by a four-probe method using a Resistivity Measurements System (RTS-8) instrument. Analysis of the porous structure was conducted with a Belsorp-max surface area detecting instrument by N_2 physisorption at 77 K (Quantachrome Instruments v4.0, America). Fourier transform infrared spectroscopic data were acquired with a Nicolet Nexus 470 infrared spectrophotometer with signal averaging of 64 scans at a resolution of 4 cm^{-1}. X-ray photoelectron spectroscopic (XPS) data were obtained with a Perkin-Elmer PHI 5000 CESCA spectrometer equipped with a hemispherical electron energy analyzer. X-ray diffraction patterns were obtained with a D8-Advance (Bruker, Germany) instrument using Cu-Kα radiation. Ultraviolet–visible (UV–vis) spectra were obtained using a UV1800 spectrophotometer (Shimadzu).

2.4 Electrochemical measurements

Electrochemical measurements were carried out in a home-made module assembled in a glove box (Mikrouna Advanced 1440/750, $H_2O < 0.1$ ppm, $O_2 <$ 0.1 ppm) under a high purity argon atmosphere. The sulfur cathode was prepared by mixing commercial elemental sulfur (Sigma-Aldrich, 99.98 wt.%), super conductive carbon black, and polytetrafluoroethylene (PTFE, Sigma-Aldrich) at weight ratios of 70/20/10 with ethanol as the dispersant. The resulting paste was rolled into ultra-thin films with approximately 1 mg of paste per 0.5 cm^2. The weight of the HCA film used for each battery was about 0.45 mg. Lithium metal (Chempur, diameter of 13 mm and thickness of 250 μm) was used as the counter electrode with polypropylene (Celgard 2300) as the separator, and 1 M lithium bis(trifluoromethanesulfonyl)imide (LiTFSI) in dioxolane/dimethoxyethane (DOL/DME, 1/1 at volume ratio) containing 0.1 M $LiNO_3$ was used as the electrolyte. The porous interlayer was placed between the sulfur cathode and the separator. The Li–S batteries were cycled using LAND CT-2001A instruments (Wuhan, China) at increasing rates from 0.2 to 4 C based on the mass and theoretical capacity of sulfur (1672 $mAh \cdot g^{-1}$) at room temperature. A voltage window in the range of 1.7 to 3.0 V was used in order to avoid the irreversible reduction of $LiNO_3$ at ~1.6 V. Cyclic voltammograms were produced by an ARBIN electrochemical workstation (MSTAT-10V/10 mA/48 Ch) at a scan rate of 0.1 mV·s^{-1}. Electrochemical impedance spectroscopy measurements were performed in the range of 100 KHz to 0.01 Hz with an AC voltage amplitude of 10 mV. Prior to long-term cycling at 1 and 2 C, the Li–S batteries were first cycled at 0.2 C for two cycles as a conditioning step. The high plateau capacity and low plateau capacity were calculated from the integrated discharge curve of the Li–S batteries with the HCA interlayer.

3 Results and discussion

The HCA was synthesized by gradually dipping a mixture of GO and CNT (Fig. S1 in the Electronic Supplementary Material (ESM)) into liquid nitrogen, followed by a freeze-drying treatment and hydrazine vapor reduction of GO and CNT (Fig. S2 in the ESM). Perpendicularly aligned ice pillars were used as templates for the production of large aligned pores (Fig. 2(a)). The formation of aligned pores was demonstrated by energy-dispersive X-ray spectroscopy using N-labeled methylene blue (Fig. S3 in the ESM) and was further verified by cross-sectional SEM (Fig. S4 in the ESM). As expected, many inter-connected mesopores were also produced from the RGO sheets and CNTs (Fig. S4 in the ESM). The porous structure could be pressed like a sponge (Fig. S5 in the ESM) without obvious structural damage. Figure 2(b) illustrates the structural differences between the HCA

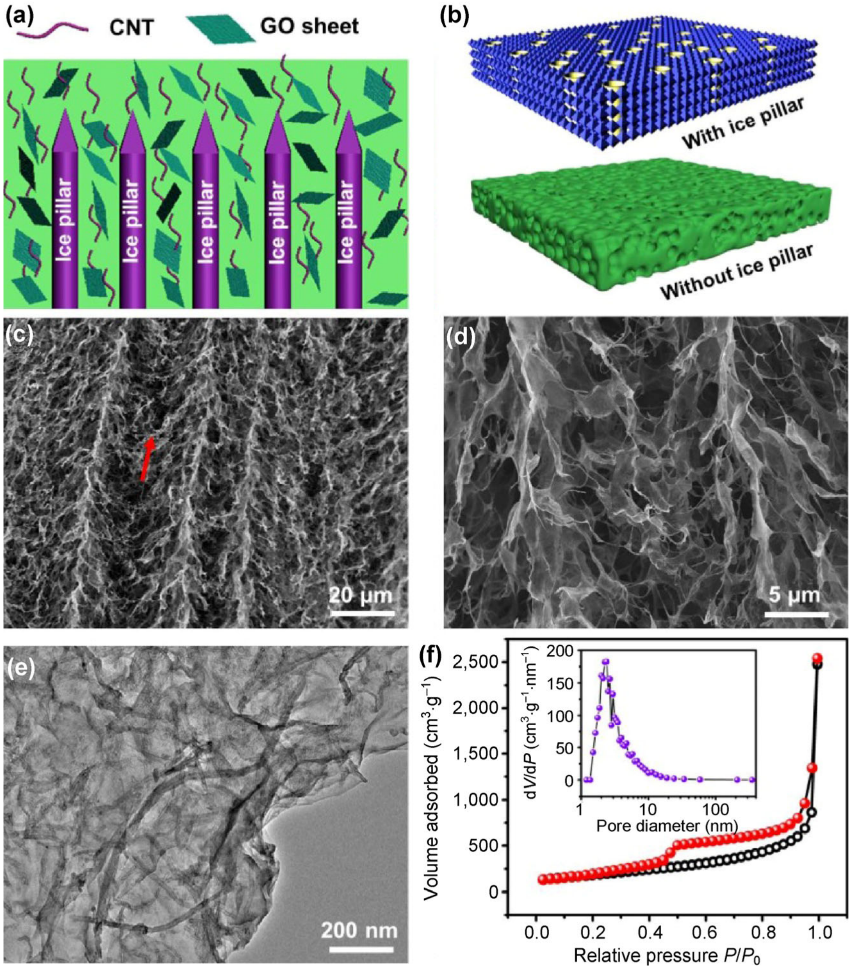

Figure 2 (a) Schematic illustration of preparation of HCA films induced by perpendicularly aligned ice pillars. (b) Schematic illustration of formation of HCA films with or without the assistance of ice pillars. (c) and (d) SEM images of porous structure of HCA film at low and high magnifications, respectively. (e) TEM image verifying uniform mixture of CNTs and RGO sheets. (f) Nitrogen adsorption/desorption isotherm and pore size distribution (inset) for HCA film.

materials formed with and without the ice pillar template. The HCA materials formed without the ice pillar template (HCA-W) had arbitrarily distributed pores without aligned pores (Fig. S6 in the ESM). For the HCA material, the aligned pores had sizes ranging from several to tens of micrometers (Fig. 2(c) and Fig. S7 in the ESM). Figure 2(d) further shows the three-dimensional framework of the HCA at high magnification, demonstrating that the RGO sheets were stacked and the CNTs were cross-linked through interfacial π−π stacking interactions and van der Waals forces [28–30]. SEM (Fig. S8 in the ESM) and TEM (Fig. 2(e)) images verified the good dispersion of the RGO sheets and CNTs without obvious aggregation. Inter-connected pores were also apparent with sizes ranging from 2 to 9 nm (inset in Fig. 2(f)), which provided a high specific surface area of 661 $m^2 \cdot g^{-1}$ (Fig. 2(f)) and a low density of ~1.28 $mg \cdot cm^{-3}$ (Fig. S9 in the ESM).

The HCA film showed a low sheet resistance of 146 $\Omega \cdot sq^{-1}$, which is comparable to that of the conductive templates comprising indium tin oxide and CNT films [31–32]. This material was integrated into an electric circuit to illuminate green light-emitting diodes (Video S1 in the ESM). In addition to the contribution of the three-dimensionally cross-linked structure, the high reduction of the GO sheets also contributed to the high electrical conductivity. The CNT and GO/CNT and RGO/CNT hybrids were compared based on Fourier transform infrared spectroscopy (Fig. S10 in the ESM). The characteristic peaks of C=O at 1,720 cm^{-1} and C–O–C at 1,228 cm^{-1} for GO [33] almost disappeared. This was also verified by X-ray diffraction. The XRD profile of HCA exhibited a broad peak at $2\theta = 26°$ with a d-spacing of 3.6 Å, compared with the sharp peak of the GO sheets centered at $2\theta = 9.4°$ with a d-spacing of 9.0 Å (Fig. S11 in the ESM), suggesting removal of the oxygenated groups and successful recovery of the π-conjugated structures upon reduction. The efficient reduction leading to recovery of the π-conjugated structure was also verified by X-ray photoelectron spectroscopy (Fig. S12 in the ESM) [28–30].

Electrochemical analysis of the Li–S battery with the HCA interlayer was performed by cyclic voltammetry (Fig. S13 in the ESM). Two peaks at 2.31 and 2.05 V were observed during the cathodic scan (Fig. S13(a) in the ESM). The first peak at 2.31 V corresponds to the conversion of elemental sulfur to long-chain soluble lithium polysulfides (Li_2S_n, $4 \leq n < 8$), while the second peak at 2.05 V is ascribed to the further reduction of lithium polysulfides to insoluble Li_2S_2 and eventually to Li_2S [17]. In the following anodic scan, two apparent oxidation peaks were observed, indicating that the oxidation process also occurred in the two previous stages. The first oxidation peak at 2.33 V is related to the formation of Li_2S_n ($n \geq 4$) from Li_2S_2 or Li_2S, and the other peak at 2.39 V is associated with the further oxidation of Li_2S_n to elemental sulfur [18]. In comparison, the cyclic voltammograms of the Li–S batteries without the HCA interlayer were characterized by inconspicuous reduction peaks and overlapping oxidation peaks (Fig. S13(b)), relative to the two characteristic peaks observed for the Li–S batteries with the HCA interlayer. The overlapping peaks may be derived from the higher over-potential obtained with pure S as the cathode, resulting in the acyclic conversion of Li_2S/Li_2S_2 and incomplete utilization of active sulfur [25, 34].

To further understand the electrochemical performance of the Li–S battery with the HCA interlayer, electrochemical analyses, including galvanostatic charge/discharge, rate capacity, long-term cycling, and electrochemical impedance spectroscopy, were performed (Fig. 3). The charge/discharge curves of the Li–S batteries with the HCA interlayers showed two obvious reduction plateaus (I and II in Fig. 3(a)), corresponding to the reduction of S_8 to long-chain polysulfides (Li_2S_n, $4 \leq n < 8$) and subsequent reduction to solid Li_2S_2/Li_2S, in accordance with the cyclic voltammograms discussed above. Accordingly, two plateaus (III and IV) were observed in the charge curves, corresponding to the reverse reaction from Li_2S/Li_2S_2 to Li_2S_4 and the oxidation of Li_2S_4 to Li_2S_8/S [23]. Due to the good interlayer effect resulting from the unique structure of HCA, the assembled Li–S battery exhibited a high discharge capacity of 1,309 $mAh \cdot g^{-1}$ at 0.2 C, which is much higher than the value of 633 $mAh \cdot g^{-1}$ for the Li–S battery without the HCA interlayer (Fig. S14 in the ESM). The assembled Li–S batteries with the HCA interlayers also displayed much higher rate capability at increasing currents

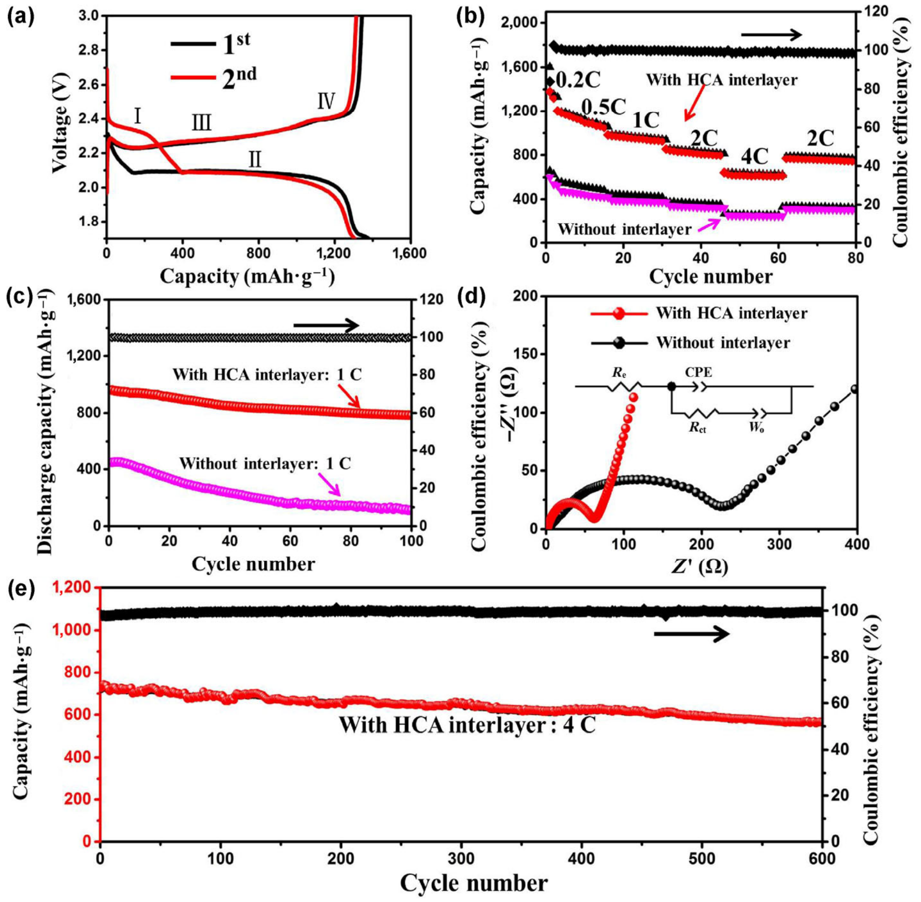

Figure 3 (a) Charge/discharge curves for first two cycles of Li–S batteries with HCA interlayer at 0.2 C. (b) and (c) Rate capability and cycling performance of Li–S batteries with and without the interlayer, respectively. (d) Nyquist plots of Li–S batteries with and without HCA interlayer before cycling and after charging to 3.0 V at 0.5 C. (e) Long-term cycling performance along with corresponding Coulombic efficiency of Li–S battery with HCA interlayer at 4 C.

from 0.5 to 4 C (Fig. 3(b)). The average discharge capacity at 4 C reached 617 mAh·g^{-1} and recovered to 785 mAh·g^{-1} when the current rate returned to 2 C, which was close to the initial value at 2 C.

As an important parameter for practical applications, the cycling performance of the assembled Li–S batteries with and without HCA interlayers was also compared (Fig. 3(c)). The Li–S batteries with HCA interlayers showed an initial discharge capacity of 944 mAh·g^{-1} at 1 C, compared to 434 mAh·g^{-1} in the case without the HCA interlayer. A high capacity retention of ~78% was achieved after 100 cycles. In strong contrast, the Li–S batteries without the HCA interlayers suffered from a sharp decrease in the capacity with 42% capacity retention after 100 cycles. Here, the Li–S cells with and without the HCA interlayer were first cycled five times in order to activate all the active sites to facilitate their complete utilization in the subsequent cycling test at a high current density of 1 C.

Electrochemical impedance spectroscopy (EIS) measurements were performed to further understand the properties of the HCA. Figure 3(d) shows the Nyquist plots of the Li–S batteries with and without HCA interlayers, along with the proposed equivalent circuit. The profiles were characterized by apparent semicircles at medium-to-high frequencies and a long inclined line corresponding to Warburg impedance (W_o) in the low frequency region. Here, the high-frequency intercept on the real axis represents the Ohmic resistance (R_e), including the electrolyte and electrode resistance in the Li–S batteries, and the semicircle comes from the interface charge transfer resistance (R_{ct}) [25]. Apparently, the semicircular region of the profile of the Li–S battery with the HCA interlayer was much smaller than that of the battery without the interlayer, indicating that introduction of the HCA interlayer can improve charge transfer at the interface between the electrode and electrolyte.

Moreover, the cycling performance achieved with the HCA interlayer was further examined at a high current density of 2 C (Fig. S15 in the ESM), and a capacity retention of ~75% was obtained after 100 cycles. In addition, the Coulombic efficiency of the Li–S battery with the HCA interlayer reached almost 100% at 2 C. A long-term test up to 600 cycles was also performed at a high current density of 4 C for the Li–S battery with the HCA interlayer (Fig. 3(e)). The sulfur electrode maintained a specific capacity of 597 $mAh\cdot g^{-1}$ with a Coulombic efficiency of ~100% after 600 cycles, and the specific capacity decayed by only 0.037% per cycle. The performance of the Li–S battery with the HCA film is comparable with that of Li–S batteries with other interlayers like carbonized paper [13], mesoporous carbon [19], carbon fiber membranes [25], and so on (Fig. 4). Figure S16 (in the ESM) presents the long-term cycling charge/discharge data, showing that the voltage curves were stable for over 600 cycles, further confirming the good cycling stability of the Li–S batteries with the HCA interlayer. Here, capacity decay mainly occurred in the low plateau (from 2.1 to 1.8 V) capacity region, corresponding to conversion of the polysulfides to lithium sulfide with capacity decay from 1,132 to 761 $mAh\cdot g^{-1}$ at 0.2 C in the first 20 cycles (Fig. 5). However, the high plateau (from 2.5 to 2.1 V) capacity region corresponding to the formation of polysulfides was stably maintained after the second round, which can be attributed to suppression of the migration of the polysulfides by the HCA interlayer when the electrolyte was saturated [35]. These results could be further confirmed by the minimal retraction of the high plateau capacity region and the marked retraction of the low plateau capacity region in the charge/discharge profiles of the Li–S battery with the HCA interlayer (Fig. S17 in the ESM). Here, the high and low plateau capacities were calculated from the integrated discharge curve of the Li–S battery with the HCA interlayer, as shown in Fig. S18 in the ESM. Moreover, the voltage intervals between the charge and discharge plateaus became slightly larger when the current was increased tenfold from 0.2 to 2 C and were stably maintained for over 100 cycles (Fig. 6). This confirmed the good rate performance of the Li–S batteries with the HCA interlayer. The relationship between the electrochemical performance and the thickness of the HCA interlayer (from 0.5 to 3.0 mm) was also investigated, as shown in Fig. S19 in the ESM, demonstrating that the thickness of the HCA film crucially affects the electrochemical performance of the Li–S batteries. The specific capacity of the sulfur cathode gradually increased as the thickness of the HCA interlayer increased. However, when the thickness of the HCA was larger than 1.5 mm, the obtained specific capacity of the Li–S battery was negatively affected. This may be due to the increased difficulty of immersion of the

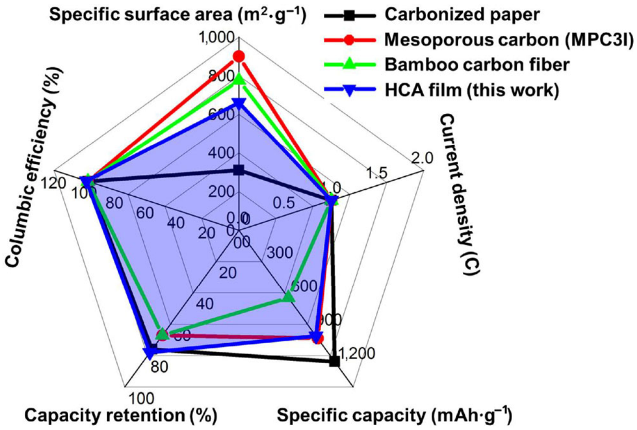

Figure 4 Comparison of performance of Li–S batteries based on HCA interlayer with Li–S batteries utilizing other interlayers [13, 19, 25].

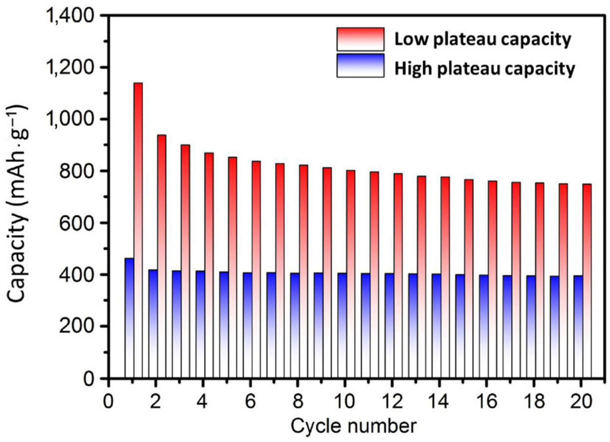

Figure 5 Galvanostatic discharge capacities at high and low voltage plateaus for Li–S battery with HCA interlayer at 0.2 C in the first 20 cycles.

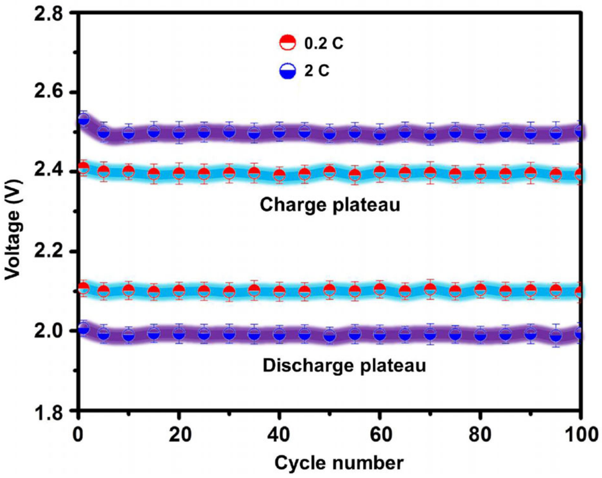

Figure 6 Voltage intervals between the charge and discharge plateaus of Li–S battery with HCA interlayer at 0.2 and 2 C.

electrolyte under such a thick or heavy interlayer, although shuttling of the polysulfides could be effectively suppressed.

Figure S20 in the ESM shows the SEM image of a cycled HCA interlayer and the corresponding carbon and sulfur elemental mapping data. The sulfur was densely and uniformly distributed over the top interface but was hardly detected at the bottom interface, proving the "capture and retain" effect of the polysulfides, which can be further used as secondary redox reaction sites for the Li+ ions according to the following equation

$$Li_2S_n\ (4 \le n < 8) + x\ Li^+ \rightarrow Li_2S_2\ /\ Li_2S \qquad (1)$$

EIS analysis was also used to study the impedance of the Li–S batteries with the HCA interlayers after 100 cycles (Fig. S21 in the ESM). The semicircle in the EIS profile of the Li–S battery with the HCA interlayer was obviously smaller than that of the Li–S battery without the HCA interlayer as a result of a decreased R_{ct} value, which favored infiltration of the electrolyte and the chemical activation process for re-distribution and dissolution of the active materials [36]. A new semicircle in the medium-frequency region emerged for the Li–S battery without the HCA interlayer, which is attributed to resistance (R_s) from the solid-electrolyte-interphase (SEI) film [37]. Here, the SEI film resulted from the thick passivation layer of irreversibly formed Li_2S, which could increase the diffusional resistance and block utilization of the interior active materials. The fitted resistances of the Li–S batteries before and after long-term cycling are summarized in Table S1 (in the ESM) and compared based on the equivalent circuit. The R_e, R_s, and R_{ct} values of the Li–S batteries with the HCA interlayers were much smaller than those without the HCA interlayers. UV–vis absorption spectra of the diluted electrolyte are presented in Fig. 7. The sharp peak at 280 nm can be attributed to the polysulfide (S_8 and S_6^{2-}) species, and the peak at 422 nm corresponds to the S_4^{2-} species [12]. The absorption peak of the Li–S battery with the HCA interlayer had lower intensity than that without the HCA interlayer, verifying the lower content of polysulfide species in the electrolyte with the barrier HCA interlayer. The "shuttle preventing" effect of the polysulfides and the mechanism of rapid transport of the electrons and lithium ions by the HCA are schematically represented in Fig. 8. The inevitably formed polysulfides were restricted from travelling to the anode side by the HCA interlayer as the tortuous pores inside the HCA films can localize the polysulfide species and accommodate the severe volume change of sulfur. In this work, HCA films as thick as 4 cm could be easily pressed into films with a network morphology (Fig. S22 in the ESM). Thus, the adequately unfolded graphene sheets with a large size of several micrometers could be pressed into networks during the assembly process, and the pore

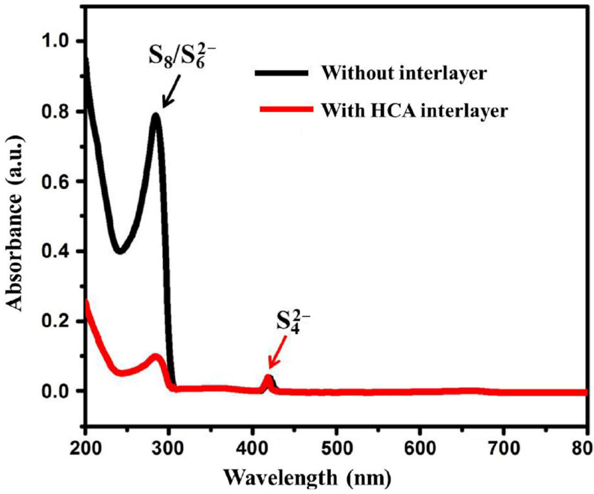

Figure 7 UV–vis absorption spectra of the solution obtained by diluting electrolytes from Li–S batteries with and without HCA interlayer in a mixture of dioxolane/dimethoxyethane (volume ratio of 1/1).

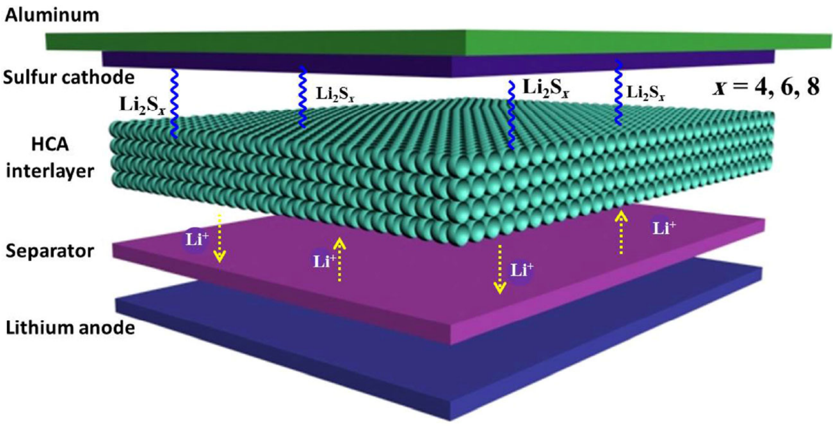

Figure 8 Schematic illustration of the "shuttle preventing" effect and rapid transport of electrons and lithium ions through the HCA film.

size of the HCA film in the Li–S batteries could be greatly decreased. This pressed HCA film can act as an effective net for suppressing shuttling of the polysulfides. Moreover, the aligned pores in the HCA film may be bent to form curved channels, as illustrated in Fig. S23 (in the ESM), and the extremely bent channels can further suppress shuttling of the polysulfide. Unfortunately, pressing of HCA interlayers without aligned pores (HCA-W) forms a compact layer without sufficient channels, which blocks the penetration of electrolyte, although the film can effectively prevent shuttling of the polysulfide.

The great improvement in the cycling performance and rate capacity can be attributed to the stable structure and high electrical conductivity of the HCA. Firstly, the HCA interlayer plays an important role in trapping the polysulfides, and dissolution and migration of the polysulfides in the electrolyte are effectively inhibited, preventing capacity fading. Secondly, the perpendicularly aligned porous structure and high electrical conductivity allow for rapid and effective transport of the electrons and lithium ions and high electrolyte immersion upon cycling, which can enhance the accessibility of the trapped active materials. Moreover, the three-dimensionally porous structure and high specific surface area of the HCA can provide sufficient space for accommodating the dramatic volume change of trapped active sulfur during the lithiation-delithiation process, ensuring high cycling stability and perfect Coulombic efficiency of the resulting Li–S batteries.

The role of the aligned pores was further carefully investigated by fabricating Li–S batteries from HCA interlayers without aligned pores (HCA-W). In the absence of the aligned pores, the Li–S batteries with the HCA-W interlayer exhibited a lower specific capacity of 986 $mAh \cdot g^{-1}$ (Fig. S24 in the ESM) compared with the Li–S battery with the HCA interlayer (1,309 $mAh \cdot g^{-1}$). Furthermore, the Li–S batteries with the HCA-W interlayer suffered from a conspicuous capacity decrease in the first 30 cycles, and presented a capacity retention of 73% after 100 cycles (Fig. S25 in the ESM). Therefore, the superior interlayer effect of the HCA material can be ascribed to the assistance of the aligned pores produced by the ice pillar template; the aligned pores were also beneficial for enhancing the performance of the resulting Li–S battery. Here, the perpendicularly aligned pores inside the HCA material may accelerate electrolyte immersion and transport of the lithium ions, resulting in rapid and sufficient utilization of the active sulfur materials. Despite the good lithium storage ability of the Li–S battery with the HCA interlayer achieved at this stage, the large volume and the non-ignorable weight (about 0.45 mg) of HCA will increase the weight of the cells and enhance the difficulty of the assembly process. Further work will be carried out in order to decrease the weight and the volume of this carbon interlayer.

As an application demonstration (Fig. 9), the Li–S battery with the HCA interlayer was used to illuminate a green light-emitting diode (LED) (ignition voltage of about 1.6 V). As a beneficial consequence of the high

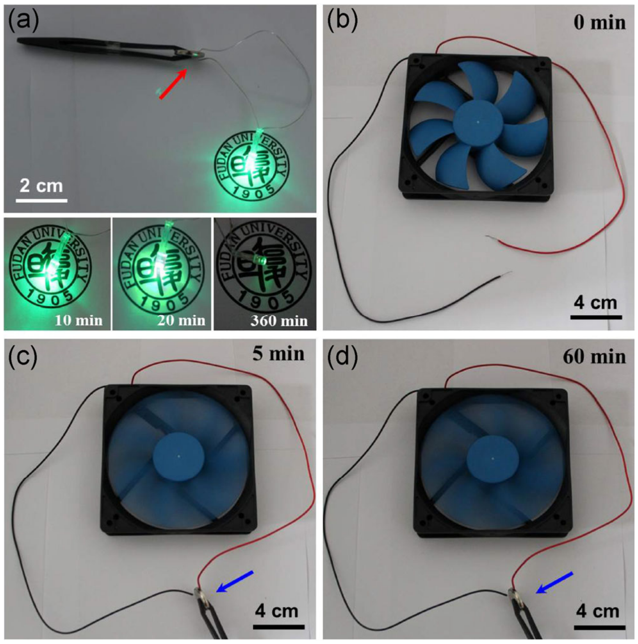

Figure 9 Demonstration of application of Li–S battery with HCA interlayer. (a) Coin Li–S battery with HCA interlayer illuminating green LED over 360 min. (b)–(d) Electric fan powered by shell Li–S battery with HCA interlayer for 60 min. Arrows in (a)–(d) indicate Li–S battery with HCA interlayer.

specific capacity and energy density, the Li–S battery with 4.9 mg of active sulfur could power the green LED for 20 min, and could still power the LED weakly for over 360 min (Fig. 9(a)). It should be noted that the Li–S battery with the HCA interlayer having an open-circuit voltage of 3.2 V could power an electric fan for up to 60 min (Figs. 9(b)–9(d)).

4 Conclusions

In summary, an electrically conductive RGO/CNT hybrid film with perpendicularly aligned macro-pores interconnected with a large number of nano-pores was created as an efficient interlayer for the Li–S battery. The three-dimensionally cross-linked structure in the hybrid film with superior mechanical toughness offers an effective prevention of "shuttling" migration of the polysulfides, affords sufficient space for the volume expansion of active sulfur, and accelerates re-utilization of the active materials. Further, due to the cross-linked structure and the high electrical conductivity of the hybrid film, rapid transport of the electrons and lithium ions among the RGO sheets through the bridged CNTs was possible (Fig. S26 in the ESM). The resulting Li–S batteries with the HCA interlayers exhibit a high specific capacity of 1,309 mAh·g^{-1} with good cyclability. This work also provides a general and promising strategy for designing hierarchically porous materials for high-performance energy storage devices.

Acknowledgements

This work was financially supported by the National Natural Science Foundation of China (Nos. 21376113, 51125011, and 51433001), Natural Science Foundation of Jiangsu Province (No. BK20150238), and the Project Funded by the Priority Academic Program Development of Jiangsu Higher Education Institutions.

Electronic Supplementary Material: Supplementary material (TEM image of CNT, cross-sectional SEM image of HCA, photographs of HCA film, FTIR spectroscopy and XRD patterns of CNT, GO/CNT and HCA, XPS spectroscopy of GO/CNT and HCA, CV curves of Li–S batteries with and without HCA interlayer, charge/discharge curves and cycling performance of Li–S battery with HCA interlayer, Nyquist plots of Li–S batteries with and without HCA interlayer after 100 cycles) is available in the online version of this article at http://dx.doi.org/10.1007/s12274-016-1244-1.

References

[1] Su, Y. S.; Fu, Y. Z.; Cochell, T.; Manthiram, A. A strategic approach to recharging lithium-sulphur batteries for long cycle life. *Nat. Commun.* **2013**, *4*, 2985.

[2] Zhao, M. Q.; Zhang, Q.; Huang, J. Q.; Tian, G. L.; Nie, J. Q.; Peng, H. J.; Wei, F. Unstacked double-layer templated graphene for high-rate lithium–sulphur batteries. *Nat. Commun.* **2014**, *5*, 3410.

[3] Yang, Z. B.; Sun, H.; Chen, T.; Qiu, L. B.; Luo, Y. F.; Peng, H. S. Photovoltaic wire derived from a graphene composite fiber achieving an 8.45% energy conversion efficiency. *Angew. Chem., Int. Ed.* **2013**, *52*, 7545–7548.

[4] Jung, D. S.; Hwang, T. H.; Lee, J. H.; Koo, H. Y.; Shakoor, R. A.; Kahraman, R.; Jo, Y. N.; Park, M. S.; Choi, J. W. Hierarchical porous carbon by ultrasonic spray pyrolysis

yields stable cycling in lithium–sulfur battery. *Nano Lett.* **2014**, *14*, 4418–4425.

[5] Fu, Y. Z.; Su, Y. S.; Manthiram, A. Highly reversible lithium/dissolved polysulfide batteries with carbon nanotube electrodes. *Angew.Chem.,Int. Ed.* **2013**, *52*, 6930–6935.

[6] Zhang, B.; Qin, X.; Li, G. R.; Gao, X. P. Enhancement of long stability of sulfur cathode by encapsulating sulfur into micropores of carbon spheres. *Energy Environ. Sci.* **2010**, *3*, 1531–1537.

[7] Li, W. Y.; Yao, H. B.; Yan, K.; Zheng, G. Y.; Liang, Z.; Chiang, Y. M.; Cui, Y. The synergetic effect of lithium polysulfide and lithium nitrate to prevent lithium dendrite growth. *Nat. Commun.* **2015**, *6*, 7436.

[8] Yin, Y. X.; Xin, S.; Guo, Y. G.; Wan, L. J. Lithium-sulfur batteries:Electrochemistry, materials, and prospects. *Angew. Chem., Int. Ed.* **2013**, *52*, 13186–13200.

[9] Yao, H. B.; Zheng, G. Y.; Hsu, P. C.; Kong, D. S.; Cha, J. J.; Li, W. Y.; Seh, Z. W.; McDowell, M. T.; Yan, K.; Liang, Z.et al. Improving lithium–sulphur batteries through spatial control of sulphur species deposition on a hybrid electrode surface. *Nat. Commun.* **2014**, *5*, 3943.

[10] Zhang, Z.; Jing, H. K.; Liu, S.; Li, G. R.; Gao, X. P. Encapsulating sulfur into a hybrid porous carbon/CNT substrate as a cathode for lithium–sulfur batteries. *J. Mater. Chem. A* **2015**, *3*, 6827–6834.

[11] Li, G. C.; Li, G. R.; Ye, S. H.; Gao, X. P. A polyaniline-coated sulfur/carbon composite with an enhanced high-rate capability as a cathode material for lithium/sulfur batteries. *Adv. Energy Mater.* **2012**, *2*, 1238–1245.

[12] Xiao, Z. B.; Yang, Z.; Wang, L.; Nie, H. G.; Zhong, M. E.; Lai, Q. Q.; Xu, X. J.; Zhang, L. J.; Huang, S. M. A lightweight TiO/graphene interlayer, applied as a highly effective polysulfide absorbent for fast, long-life lithium–sulfur batteries. *Adv. Mater.* **2015**, *27*, 2891–2898.

[13] Chung, S. H.; Manthiram, A. A hierarchical carbonized paper with controllable thickness as a modulable interlayer system for high performance Li–S batteries. *Chem. Commun.* **2014**, *50*, 4184–4187.

[14] Yan, J. H.; Li, B. Y.; Liu, X. B. Nano-porous sulfur-polyaniline electrodes for lithium-sulfurbatteries. *Nano Energy* **2015**, *18*, 245–252.

[15] Yan, J. H.; Liu, X. B.; Yao, M.; Wang, X. F.; Wafle, T. K.; Li, B. Y. Long-life, high-efficiency lithium-sulfur battery from a nanoassembled cathode. *Chem. Mater.* **2015**, *27*, 5080–5087.

[16] Yan, J. H.; Liu, X. B.; Qi, H.; Li, W. Y.; Zhou, Y.; Yao, M.; Li, B. Y. High-performance lithium-sulfur batteries with a cost-effective carbon paper electrode and high sulfur-loading. *Chem. Mater.* **2015**, *27*, 6394–6401.

[17] Huang, Y.; Zheng, M. B.; Lin, Z. X.; Zhao, B.; Zhang, S. T.; Yang, J. Z.; Zhu, C. L.; Zhang, H.; Sun, D. P.; Shi, Y. Flexible cathodes and multifunctional interlayers based on carbonized bacterial cellulose for high-performance lithium–sulfur batteries. *J. Mater. Chem. A* **2015**, *3*, 10910–10918.

[18] Zhou, G. M.; Pei, S. F.; Li, L.; Wang, D. W.; Wang, S. G.; Huang, K.; Yin, L. C.; Li, F.; Cheng, H. M. A graphene-pure-sulfur sandwich structure for ultrafast, long-life lithium-sulfur batteries. *Adv. Mater.* **2014**, *26*, 625–631.

[19] Balach, J.; Jaumann, T.; Klose, M.; Oswald, S.; Eckert, J.; Giebeler, L. Mesoporouscarbon interlayers with tailored pore volume as polysulfide reservoir for high-energy lithium–sulfur batteries. *J. Phys. Chem. C* **2015**, *119*, 4580–4587.

[20] Yan, J. H.; Liu, X. B.; Wang, X. F.; Li, B. Y. Long-life, high-efficiency lithium/sulfur batteries from sulfurized carbon nanotube cathodes. *J. Mater. Chem. A* **2015**, *3*, 10127–10133.

[21] Singhal, R.; Chung, S. H.; Manthiram, A.; Kalra, V. A free-standing carbon nanofiber interlayer for high-performance lithium–sulfur batteries. *J. Mater. Chem. A* **2015**, *3*, 4530–4538.

[22] Song, J. X.; Yu, Z. X.; Xu, T.; Chen, S. R.; Sohn, H. S.; Regula, M.; Wang, D. H. Flexible freestanding sandwich-structured sulfur cathode with superior performance for lithium–sulfur batteries. *J. Mater. Chem. A* **2014**, *2*, 8623–8627.

[23] Su, Y. S.; Manthiram, A. A new approach to improve cycle performance of rechargeable lithium–sulfur batteries by inserting a free-standing MWCNT interlayer. *Chem. Commun.* **2012**, *48*, 8817–8819.

[24] Lee, C. L.; Kim, I. D. A hierarchical carbon nanotube-loaded glass-filter composite paper interlayer with outstanding electrolyte uptake properties for high-performance lithium–sulphur batteries. *Nanoscale* **2015**, *7*, 10362–10367.

[25] Gu, X. X.; Lai, C.; Liu, F.; Yang, W. L.; Hou, Y. L.; Zhang, S. Q. A conductive interwoven bamboo carbon fiber membrane for Li–S batteries. *J. Mater. Chem. A* **2015**, *3*, 9502–9509.

[26] Wang, B.; Wen, Y. F.; Ye, D. L.; Yu, H.; Sun, B.; Wang, G. X.; Hulicova-Jurcakova, D.; Wang, L. Z. Dual protection of sulfur by carbon nanospheres and graphene sheets for lithium-sulfur batteries. *Chem.—Eur. J.* **2014**, *20*, 5224–5230.

[27] Chung, S. H.; Manthiram, A. Bifunctionalseparator with a light-weight carbon-coating for dynamically and statically stable lithium-sulfur batteries. *Adv. Funct. Mater.* **2014**, *24*, 5299–5306.

[28] Sun, H. Y.; Xu, Z.; Gao, C. Multifunctional, ultra-flyweight, synergistically assembled carbon aerogels. *Adv. Mater.* **2013**, *25*, 2554–2560.

[29] Xu, Z.; Liu, Z.; Sun, H. Y.; Gao, C. Highly electrically conductive Ag-doped graphene fibers as stretchable conductors. *Adv. Mater.* **2013**, *25*, 3249–3253.

[30] Xu, Z.; Zhang, Y.; Li, P. G.; Gao, C. Strong, conductive,

lightweight, neat graphene aerogel fibers with aligned pores. *ACS Nano* **2012**, *6*, 7103–7113.

[31] Bae, S.; Kim, H.; Lee, Y. B.; Xu, X. F.; Park, J. S.; Zheng, Y.; Balakrishnan, J.; Lei, T.; Ri Kim, H.; Song, Y. I. et al. Roll-to-roll production of 30-inch graphene films for transparent electrodes. *Nat. Nanotechnol.* **2010**, *5*, 574–578.

[32] Lee, J. Y.; Connor, S. T.; Cui, Y.; Peumans, P. Solution-processed metal nanowire mesh transparent electrodes. *Nano Lett.* **2008**, *8*, 689–692.

[33] Mi, X.; Huang, G. B.; Xie, W. S.; Wang, W.; Liu, Y.; Gao, J. P. Preparation of graphene oxide aerogel and its adsorption for Cu^{2+} ions. *Carbon* **2012**, *50*, 4856–4864.

[34] Li, D.; Han, F.; Wang, S.; Cheng, F.; Sun, Q.; Li, W. C. High sulfur loading cathodes fabricated using peapodlike, large pore volume mesoporous carbon for lithium–sulfur battery. *ACS Appl. Mater. Interfaces* **2013**, *5*, 2208–2213.

[35] Fang, X.; Weng, W.; Ren, J.; Peng, H. S. A cable-shaped lithium sulfur battery. *Adv. Mater.* **2016**, *28*, 491–496.

[36] Gu, X. X.; Wang, Y. Z.; Lai, C.; Qiu, J. X.; Li, S.; Hou, Y. O.; Martens, W.; Mahmood, N.; Zhang, S. Q. Microporous bamboo biochar for lithium-sulfur batteries. *Nano Res.* **2015**, *8*, 129–139.

[37] Wang, W. G.; Wang, X.; Tian, L. Y.; Wang, Y. L.; Ye, S. H. *In situ* sulfur deposition route to obtain sulfur–carbon composite cathodes for lithium–sulfur batteries. *J. Mater. Chem. A* **2014**, *2*, 4316–4323.